# Ag$_3$PO$_4$/Ti$_3$C$_2$ MXene interface materials as a Schottky catalyst with enhanced photocatalytic activities and anti-photocorrosion performance

Tao Cai[a,b], Longlu Wang[c], Yutang Liu[a,b,*], Shuqu Zhang[c], Wanyue Dong[a,b], Hui Chen[a,b], Xuanying Yi[c], Jili Yuan[c], Xinnian Xia[d,**], Chengbin Liu[c], Shenglian Luo[c]

[a] College of Environmental Science and Engineering, Hunan University, Lushan South Road, Yuelu District, Changsha 410082, PR China
[b] Key Laboratory of Environmental Biology and Pollution Control (Hunan University), Ministry of Education, Lushan South Road, Yuelu District, Changsha 410082, PR China
[c] State Key Laboratory of Chemo/Biosensing and Chemometrics, Hunan University, Lushan South Road, Yuelu District, Changsha 410082, PR China
[d] College of Chemistry and Chemical Engineering, Hunan University, Changsha 410082, PR China

## ARTICLE INFO

## ABSTRACT

The high carrier recombination rate and serious photocorrosion of Ag$_3$PO$_4$ greatly restrict its photocatalytic application. Here, we fabricated an Ag$_3$PO$_4$/Ti$_3$C$_2$ Schottky catalyst and found that Ti$_3$C$_2$ can greatly enhanced the catalytic activity and stability of Ag$_3$PO$_4$. This arises from: (i) the abundant surface hydrophilic functional groups of Ti$_3$C$_2$ construct strong interfacial contact with Ag$_3$PO$_4$, which facilitate the separation of carriers; (ii) the strong redox reactivity of surface Ti sites promote multiple electron reduction reactions to induce more ·OH production; and (iii) a Schottky junction formed at Ag$_3$PO$_4$-Ti$_3$C$_2$ interface timely transfer electrons to Ti$_3$C$_2$ surface by built-in electric field, inhibiting the photocossion of Ag$_3$PO$_4$ caused by photogeneration electrons. Consequently, Ag$_3$PO$_4$/Ti$_3$C$_2$ exhibited excellent photocatalytic activity and stability for the degradation of organic pollutants. Especially, the apparent rate constant of 2,4-Dinitrophenol degradation with Ag$_3$PO$_4$/Ti$_3$C$_2$ was 2.5 times that of Ag$_3$PO$_4$/RGO and 10 times that of Ag$_3$PO$_4$. The photocatalytic performance of Ag$_3$PO$_4$/Ti$_3$C$_2$ toward tetracycline hydrochloride still maintained 68.4% after 8 cycles, while Ag$_3$PO$_4$/RGO and Ag$_3$PO$_4$ only maintained 36.2% and 7.8%, respectively. Furthermore, the efficient photoreduction of Cr$^{6+}$ using AgI/Ti$_3$C$_2$ further illustrated an enormous potential in coupling Ti$_3$C$_2$ with other photosensitivity semiconductor to improve their catalytic activity and stability.

## 1. Introduction

Photocatalysis has attracted great interest in resolving environmental problems caused by heavy metal ion (e.g., Cr$^{6+}$, Pb$^{2+}$, etc.) and organic pollutants (e.g., antibiotics, persistent organic pollutant, dyes, etc.) [1–3]. Silver-based semiconductors (such as Ag$_3$PO$_4$, AgBr and AgI, etc) are emerging as a class of high-effective catalysts for the removal of organic contaminants [4–10]. Among them, it is considered that Ag$_3$PO$_4$ has the highest quantum efficiency of about 90% at the wavelengths around 420 nm in water oxidation [11–13]. Although Ag$_3$PO$_4$ exhibits high-efficient visible-light photocatalytic performance, its degradation performance toward organic pollutants still needs to be improved. One reason is that the carrier recombination rate is relatively high and the potential of the conduction band (CB) is relatively low [14]. Another reason is that Ag$_3$PO$_4$ is easily decomposed into the silver

by the photogenerated electrons during the photocatalytic process (Photocorrosion: $4Ag_3PO_4 + 6H_2O + 12h^+ + 12e^- \rightarrow 12Ag^+ + 4H_3PO_4 + 3O_2$) [4,15]. These problems severely limit its practical application.

In order to solve above issues, Ag$_3$PO$_4$ based hybrid materials including Ag$_3$PO$_4$/graphene [16,17], Ag$_3$PO$_4$/BiVO$_4$ [18], Ag$_3$PO$_4$/g-C$_3$N$_4$ [19,20], AgX/Ag$_3$PO$_4$ [21], Ag$_3$PO$_4$/NiFe$_2$O$_4$ [22], etc. had been largely studied. Photocatalytic performance of these Ag$_3$PO$_4$-based composites were improved because of the reduced charge carrier recombination. Among them, two-dimensional (2D) layer materials (eg., graphene and g-C$_3$N$_4$.) have been considered as the most promising candidate for heterogeneous catalysis due to ultrahigh electron mobility [23,24] and large surface area [25], etc. However, several issues caused by the intrinsic properties of current 2D layer materials still exist: (i) These layer materials only provided weak and smaller contact between
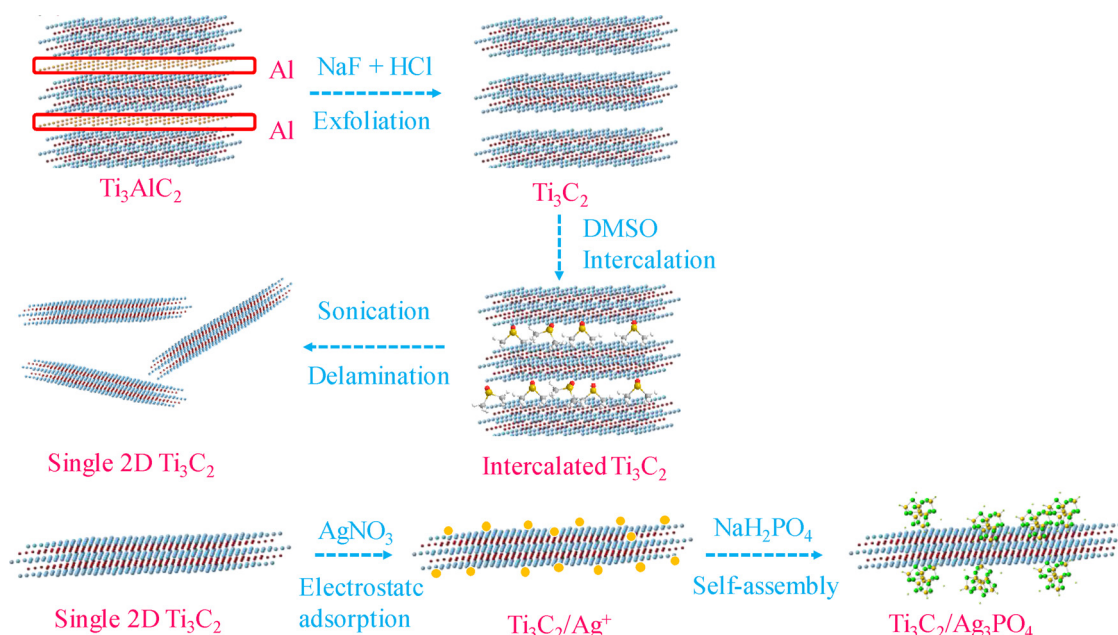
---

**Fig. 1.** Schematic representation of single 2D $Ti_3C_2$ sheets and $Ag_3PO_4/Ti_3C_2$ synthesis.

the bulk phases and $Ag_3PO_4$, which usually result in low conjunction of interface. The lower and weaker conjunction could significantly restrict the separation of charge carriers [26]; (ii) The oxidation of graphene could weaken the electronic conductivity for carriers transmission [4]; (iii) The electronic properties of graphene oxide (GO) can also be easily disrupted during the reduction process (The destruction of π-conjugated system) [27]. Thus, it is highly desirable to find new materials that can overcome these shortcomings.

MXene, two-dimensional (2D) early transition metal carbides, nitrides or carbonitrides, are widely used in batteries [28–30] and supercapacitors [31,32]. Moreover, recent studies have shown that $Ti_3C_2$ MXene has great potential as a co-catalyst for photocatalytic hydrogen production [33,34]. Notably, its unique natures render it extremely promising for handling the above issues as: (i) $Ti_3C_2$ MXene possesses a large number of hydrophilic functional groups (eg., –O and −OH) on its surface, making it easy to build a strong and sufficient connection with $Ag_3PO_4$ or other semiconductors; (ii) The surface terminal Ti sites might result in much stronger redox reactivity than that of traditional carbon materials [35]; (iii) The prominent metallic conductivity of $Ti_3C_2$ MXene make it to be an excellent "electron sink" for efficient carriers transfer. Considering the above excellent properties of the $Ti_3C_2$ MXene, it is expected that the combination of $Ti_3C_2$ MXene and $Ag_3PO_4$ can significantly improve the photocatalytic performance and stability of $Ag_3PO_4$. Moreover, since $Ti_3C_2$ MXene has excellent metallic conductivity, a Schottky junction may be formed at $Ti_3C_2$-$Ag_3PO_4$ interface, which usually formed at the semiconductor-metal interface. Schottky junctions are generally introduced to generate the built-in electric field, which has been recognized as an effective strategy to improve carrier separation [36]. In this regard, designing a $Ti_3C_2$ MXene based Schottky catalyst to achieve more high-efficient photocatalytic activity is very desirable, but still waiting to be studied.

Herein, we synthesized an $Ag_3PO_4/Ti_3C_2$ MXene Schottky catalyst by electrostatically driven self-assembly strategy successfully. The photocatalytic activity and anti-photocorrosion performance of the $Ag_3PO_4/Ti_3C_2$ MXene Schottky catalyst were evaluated by the degradation of antibiotics and persistent organic pollutant (POPs). Compared with typical $Ag_3PO_4/RGO$ and pure $Ag_3PO_4$, it showed preferable photocatalytic activity and anti-photocorrosion performance. The origin of this high activity and stability was studied systematically. Considering the complex composition of actual water bodies, the

influences of diverse inorganic ion (eg., $Na^+$, $SO_4^{2-}$ and $NO_3$-, etc.) and natural organic matters (NOMs) on its photocatalytic properties were also studied. Moreover, the efficient photoreduction of $Cr^{6+}$ using AgI/$Ti_3C_2$ further demonstrated that the considerable potential of $Ti_3C_2$ MXene as an "electron sink" for the construction of Schottky junction to improve catalytic activity and stability of photosensitivity semiconductors.

## 2. Experimental

### 2.1. Chemicals

All chemicals (analytic grade reagents) used were purchased from Sinopharm Chemical Reagent Co. Ltd and without further purification. Deionized water (D.I. water) was prepared by ULUPURE purification system and used throughout the experiments.

### 2.2. Materials synthesis

#### 2.2.1. Preparation of single $Ti_3C_2$ MXene sheet

$Ti_3C_2$ MXene was fabricated by immersing $Ti_3AlC_2$ in etching solutions. The etching solution was prepared by mixing NaF (3.35 g) with HCl solution (20 mL, 36–38 wt.%) according to the previous report [37]. Briefly, 0.5 g $Ti_3AlC_2$ was dispersed in 20 ml etching solution, and then kept for 12 h at 60 °C with continuous stirring. Thereafter the precipitate was washed by diluted hydrochloric acid (2 mol/L), ethanol and D.I. water several times, and separated by centrifugation. Finally, the obtained MXene powder was dried in vacuum at 80 °C. Single $Ti_3C_2$ sheets were performed using dimethyl sulfoxide (DMSO) intercalation method [38]. 0.3 g of $Ti_3C_2$ was dispersed into 5 ml DMSO with continuous stirred for 24 h and then a black powder was obtained. Thereafter the powder was immersed in D.I. water and then sonication for 6 h. Finally, single $Ti_3C_2$ MXene sheets were obtained by filtering through a porous anodic alumina membrane filter.

#### 2.2.2. Preparation of $Ag_3PO_4/Ti_3C_2$

$Ag_3PO_4/Ti_3C_2$ was prepared by an electrostatically driven self-assembly method. Firstly, a certain amount of $Ti_3C_2$ sheets were dispersed into D.I. water and sonicated for 30 min to get a $Ti_3C_2$ suspension. Secondly, 10 mL, 0.6 M $AgNO_3$ aqueous solution was added to the

above $Ti_3C_2$ suspension with vigorous stirring for 15 min. And then $Na_2HPO_4$ aqueous solution (10 mL, 0.2 M) was added dropwise to the mixture with keeping stirring for 2 h. Finally, the obtained precipitate was washed with D.I. water several times and dried in vacuum (80 °C) overnight. The detail preparation flowchart of $Ti_3C_2$ and $Ag_3PO_4/Ti_3C_2$ was provided in Fig. 1.

### 2.2.3. Preparation of $Ag_3PO_4$, $Ag_3PO_4/GO$ and $Ag_3PO_4/RGO$

According to a typical synthesis method [16], $Na_2HPO_4$ aqueous solution (10 mL, 0.2 M) was slowly added dropwise to the $AgNO_3$ aqueous solution (10 mL, 0.6 M) with magnetically stirring, until the solution turned golden. The precipitate was collected, washed with D.I. water several times, and dried in vacuum (80 °C) overnight. GO was prepared by the improved Hummers method [39]. $Ag_3PO_4/GO$ was prepared by the above electrostatically driven self-assembly method. $Ag_3PO_4/RGO$ was obtained by directly photoreduction ($\lambda > 420$ nm) of $Ag_3PO_4/GO$ aqueous solution containing ethanol (5%, v/v) for 15 min.

### 2.2.4. Preparation of AgI and $AgI/Ti_3C_2$

AgI was prepared by the direct reaction of $AgNO_3$ and NaI at room temperature. Briefly, NaI aqueous solution (10 mL, 0.2 M) was slowly added to the $AgNO_3$ aqueous solution (10 mL, 0.2 M) under magnetically stirring condition. After 30 min of reaction, the precipitate was collected, washed with D.I. water several times, and dried in vacuum (80 °C) overnight. $AgI/Ti_3C_2$ was also synthesized by the above electrostatically driven self-assembly method.

### 2.3. Characterization

The X-ray diffraction (XRD) with Cu-Kα radiation (Rigaku, Smartlab) at a scanning rate of 5 min$^{-1}$ in the $2\theta$ range of 5–80°, and X-ray photoelectron spectroscopy (XPS) with Al-Kα X-ray ($h\nu = 1486.6$ eV) radiation (Thermo Fisher Scientific, England) were used to determine the crystal structures and chemical composition of samples. All of the binding energies were calibrated by C 1s peak at 484.8 eV. The field emission scanning electron microscopy (FE-SEM) (Hitachi, S-4800) and transmittance electron microscopy (TEM) (JEOL, JEM-2100F) were used to observe the morphologies. Energy dispersive X-ray spectroscopy (EDX) was collected by TEM (JEOL, JEM-2100 F). Raman spectra was acquired on a DXR spectrometer with the 532 nm laser. The UV–vis diffuse-reflectance spectra (DRS) was recorded using UV–vis spectrophotometer (Cary 300, Varian) with $BaSO_4$ as the background. The photoluminescence (PL) spectra was acquired on Hitachi F-7000 fluorescence spectrophotometer with the excitation wavelength of 310 nm, scanning speed of 240 nm/min and PMT voltage of 650 V. The time-resolved PL spectra was tested in a single photon counting system. Bandgap excitation was triggered by a sub-nanosecond pulsed diode laser ($\lambda = 295$ nm, PicoQuant).

Photoelectrochemical measurements were performed in 0.5 M $Na_2SO_4$ electrolyte solution in a typical three-electrode system (A working electrode, a platinum wire counter electrode and a Ag/AgCl reference electrode). The CHI 660C electrochemical analyzer (CHI Inc., USA) was use to record the electrochemical response. During the test of transient photocurrent, the working electrodes were prepared by coating the $Ag_3PO_4$, $Ag_3PO_4/RGO$ and $Ag_3PO_4/Ti_3C_2$ samples on fluorine doped tin oxide (FTO) conductive glass, and then immersed into 0.5 M $Na_2SO_4$ aqueous solution. A 300 W Xe lamp was used as the light source. Mott-Schottky test was carried out under direct current potential polarization at different fixed frequencies of 1000 Hz, 2000 Hz and 3000 Hz. Nafion was used as the adhesive during the prepare process of working electrodes. Electron spin resonance (ESR) spectra was carried out on a JES FA200 electron paramagnetic resonance spectrometer. Instrument settings: center field, 3232 G; sweep width, 50 G; sweep time, 1 min; modulation frequency, 100 kHz; microwave power, 1 mW; microwave frequency, 9.05 GHz.

### 2.4. Photocatalytic performance measurement

#### 2.4.1. Photodegradation of organic pollutants under visible light irradiation

The photodegradation of organic pollutants using as-prepared catalyst was performed under visible light irradiation (300 W Xe lamp with a cut off filter, $\lambda > 420$ nm). Typically, 20 mg of as-prepared catalyst was added into the reaction solution (50 mL, 20 mg/L methyl orange (MO), 2,4-Dinitrophenol (2,4-DNP), tetracycline hydrochloride (TC-H), thiamphenicol (TPL) or chloramphenicol (CPL)) with stirring for 30 min under dark environment to reach an adsorption-desorption equilibrium. During the photodegradation, 1 mL of suspension was taken out at a given interval time and separated through centrifugation (3000 rpm, 8 min) for further analysis.

#### 2.4.2. Photoreduction of $Cr^{6+}$ under visible light irradiation

The 50 mL $K_2Cr_2O_7$ solution with the concentration of 10 mg/L was employed as the pollutant for this test. 20 mg as-prepared catalyst was added into the $K_2Cr_2O_7$ solution. After reaching an adsorption-desorption equilibrium, the photoreduction of $Cr^{6+}$ was conducted under visible light irradiation. The sample aliquot was intermittently withdrawn and separated through centrifugation (3000 rpm, 8 min) for further analysis.

### 2.5. Analysis

The concentration of $Cr^{6+}$ was measured by the DPC (diphenylcarbazide) method [40]. The concentration of thiamphenicol (TPL) and chloramphenicol (CPL) was analyzed by a high-performance liquid chromatograph (HPLC, Shimadzu LC-20AT), which using a phenomenex Luna C-18 column and a SPD-20 A UV/Vis detector at 278 nm, with methanol and water (65/35, v/v) as effluent at a flow rate of 0.8 mL/min. The concentration of methyl orange (MO), 2,4-Dinitrophenol (2,4-DNP) and tetracycline hydrochloride (TC-H) was determined by the characteristic optical absorption at 465 nm, 370 nm and 357 nm, respectively with a UV–vis spectrophotometer (CARY 300 Conc).

## 3. Results and discussion

### 3.1. Structural investigations

The crystal structure of as-prepared catalysts were thoroughly investigated by X-ray diffraction (XRD). Obvious diffraction peaks associated with the $Ti_3AlC_2$ crystals were found and the (002) peak and (104) peak of $Ti_3AlC_2$ completely disappeared after etching (Fig. 2a). New peaks at 9°, 24.3° and 48° were observed, indicating that $Ti_3AlC_2$ completely converted to $Ti_3C_2$ [29,41]. All the diffraction peaks in pure $Ag_3PO_4$, $Ag_3PO_4/RGO$ and $Ag_3PO_4/Ti_3C_2$ samples could be indexed to the typical body-centered cubic structure (JCPDS NO.06-0505) (Fig. 2(a, b)). A combination of $Ti_3C_2$ or RGO with $Ag_3PO_4$ did not affect the crystal structure of $Ag_3PO_4$, excluding the influence of the crystal structure on catalytic activity. Attributing to the relatively low amount and high dispersion of $Ti_3C_2$ and RGO, there were no notable characteristic diffraction peaks of $Ti_3C_2$ and RGO in the XRD pattern [16,33]. RGO was obtained by the reduction of GO. As shown in Fig. S1, The D/G intensity ratio (D peak at 1350 cm$^{-1}$ and G peak at 1590 cm$^{-1}$) increases from 1.01 to 1.12, indicating the transform of GO to RGO [42]. The photo images of $Ti_3C_2$ and RGO were also provided in Fig. S2. Notably, a small amount of metallic Ag appeared in the XRD pattern of $Ag_3PO_4/Ti_3C_2$, which might be due to the Ag self-reduction in $Ti_3C_2$ MXene solution caused by low valence Ti [43,44]. Moreover, no any other trace of impurities were appeared in the pattern, suggesting the formation of pure $Ag_3PO_4$ and $Ti_3C_2$ crystal structure.

The morphologies of the as-prepared samples were investigated by (HR)TEM and SEM techniques. The formed accordion-like multilayer nanostructure reveal the typical MXene morphology (Figs. 3a and S3a)
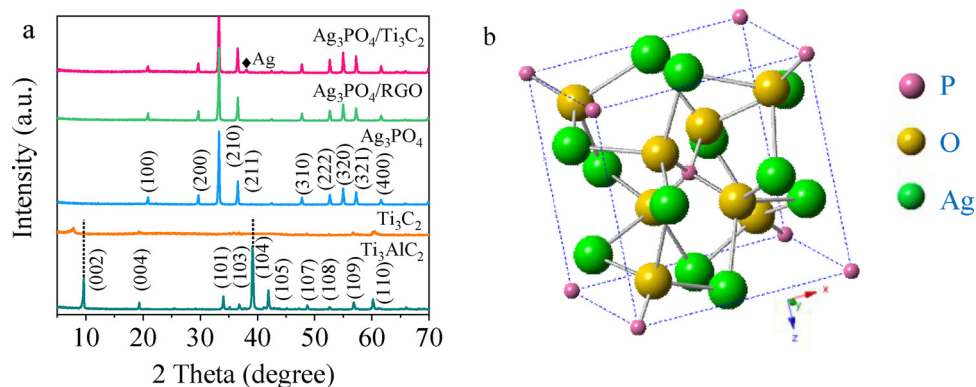
**Fig. 2.** (a), X-ray diffraction (XRD) patterns of the as-prepared catalysts. (b), Crystal structure model of $Ag_3PO_4$.

[45]. After delaminating, single $Ti_3C_2$ sheets were obtained with a relatively broad size (Figs. 3b and S3b), which may provide more nucleation sites for the crystal growth of $Ag_3PO_4$. HRTEM image of $Ti_3C_2$ (inset in Fig. 3b) showed a lattice spacing of about 0.266 nm, which was assigned to the (010) plane of $Ti_3C_2$ [46]. After combined with $Ag_3PO_4$ particles (ca. 100–200 nm), the $Ti_3C_2$ sheets are completely wrapped on these particles (Figs. 3c and S3c). This can be attributed to the electrostatically-driven self-assembly between $Ag^+$ and negatively charged $Ti_3C_2$ sheets. Note that the presence of $Ti_3C_2$ caused a slight decrease in the sizes of $Ag_3PO_4$ particles in the $Ag_3PO_4/Ti_3C_2$ composites compared with pure $Ag_3PO_4$ (Fig. S3 (c, d)). The results imply that $Ti_3C_2$ play an important role in the morphology and size control of $Ag_3PO_4$ particles, which is beneficial for photocatalytic process. The corresponding EDX spectrum in Fig. 3d indicated that $Ag_3PO_4/Ti_3C_2$ contained Ag, P, Ti, O and C and no any other impurities elements, which was consistent with the XRD result. For comparison, $Ag_3PO_4/RGO$ was prepared by the same method, which exhibited similar morphology with $Ag_3PO_4/Ti_3C_2$ (Fig. S4), indicating that the difference in catalytic activity is not caused by the morphology.

Fig. 4a showed the survey XPS spectrum of $Ag_3PO_4$, $Ti_3C_2$ and $Ag_3PO_4/Ti_3C_2$. The binding energies of the samples were calibrated at 284.8 eV with respect to the carbon (C 1 s) as a reference line. All signals of Ag, P, O, C, and Ti were clearly observed in the survey XPS spectrum of $Ag_3PO_4/Ti_3C_2$, which was consistent with the EDX result. Four peaks at 288.9, 286.7, 284.8 and 281.3 eV can be deconvoluted in the C 1 s pattern of $Ti_3C_2$ (Fig. 4b), which are ascribed to C−F, C−O, C−C and C−Ti bonds, respectively [47]. After the combination of $Ti_3C_2$ with $Ag_3PO_4$, the peaks of C−F and C−O were greatly decreased, implying a strong interaction between $Ag_3PO_4$ and $Ti_3C_2$. Because the abundant surface termination groups render negatively charged surface for $Ti_3C_2$ [33,48], which makes the connection of $Ti_3C_2$ with $Ag_3PO_4$ easier. It should be noted that the peak of C−Ti was disappeared in $Ag_3PO_4/Ti_3C_2$, indicating that part C−Ti bond was broken during the synthetic process. In the case of the Ti 2p pattern of $Ti_3C_2$, six peaks at 454.6, 456.2, 458.9, 460.8, 462.7 and 464.9 eV can be deconvoluted, which are ascribed to Ti(III) $2p_{3/2}$, Ti(II) $2p_{3/2}$, Ti(IV) $2p_{3/2}$, Ti(II) $2p_{1/}$
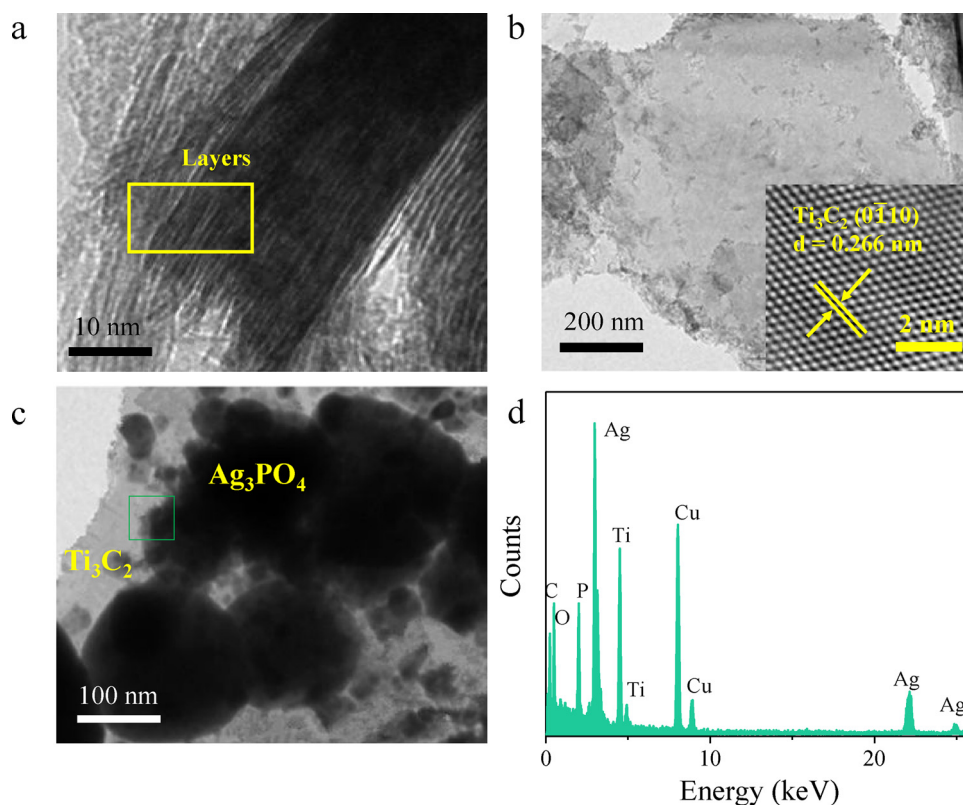


**Fig. 3.** TEM images of (a) bulk $Ti_3C_2$, (b) single $Ti_3C_2$ sheet and (c) $Ag_3PO_4/Ti_3C_2$ composite. (d) EDX spectrum of $Ag_3PO_4/Ti_3C_2$ composite.

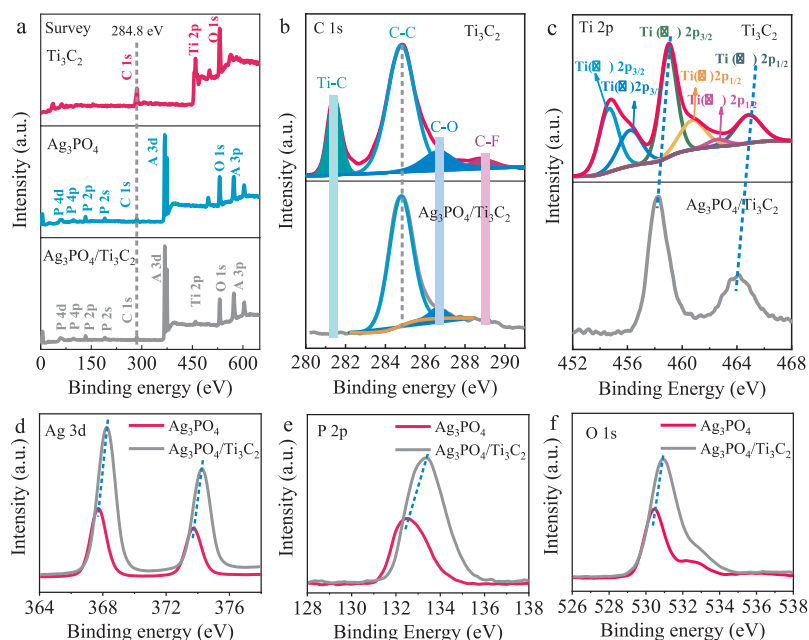**Fig. 4.** (a), Survey XPS spectrum of as-prepared catalysts. High-resolution XPS spectrum of C 1 s (b) and Ti 2p (c) of $Ti_3C_2$ and $Ag_3PO_4/Ti_3C_2$ composite. High-resolution XPS spectrum of Ag 3d (d), P 2p (e) and O 1 s (f) of $Ag_3PO_4$ and $Ag_3PO_4/Ti_3C_2$ composite.

$_2$, Ti(III) $2p_{1/2}$ and Ti(IV) $2p_{1/2}$, respectively [44,49]. Such low valence Ti species with strong reductive activity could as electron donors to conduct reduction reaction [44]. After compounding with $Ag_3PO_4$, the peaks corresponding low valence Ti species were completely disappeared, indicating that the intense redox reaction occurred during the synthetic process due to the consume of low valence Ti species. This may explain why a small amount of metallic Ag appeared in the XRD pattern of $Ag_3PO_4/Ti_3C_2$. Notably, a negative shift of Ti(IV) $2p_{3/2}$ and Ti(IV) $2p_{1/2}$ peaks were observed on $Ag_3PO_4/Ti_3C_2$ compared with $Ti_3C_2$. However, Ag 3d, P 2p and O 1s peaks in $Ag_3PO_4/Ti_3C_2$ moved to positive position (Fig. 4d, e and f). In general, the binding energy is negatively related to surface electron density [36]. Thus, XPS results indicated that electrons were transferred from $Ag_3PO_4$ to the $Ti_3C_2$ surface after $Ti_3C_2$ and $Ag_3PO_4$ contact, which lead to the formation of Schottky junction between $Ti_3C_2$-$Ag_3PO_4$ interface. Schottky junctions could generate a built-in electric field, improving carriers separation rate greatly. This will be discussed detailly in mechanism section.

### 3.2. Photoelectric properties and band structure determination

Fig. 5a presented the UV–vis diffuse reflectance spectra for as-prepared samples. All samples exhibited excellent absorption in the region less than 500 nm. Specially, there was a distinct enhanced absorbance from approximately 500 nm to 800 nm for both $Ag_3PO_4/Ti_3C_2$ and $Ag_3PO_4/RGO$ composite compared with pure $Ag_3PO_4$, indicating that both $Ti_3C_2$ and RGO sheets successfully coupling with $Ag_3PO_4$. Since $Ti_3C_2$ and RGO covered on the surface of the $Ag_3PO_4$, the light absorption will be reduced to some extent. Thus, it is necessary to evaluate the transmittance of materials. $Ti_3C_2$ and RGO films with the same thickness were prepared by spin-coating method on the surface of FTO. As shown in Fig.5b, $Ti_3C_2$ had better transmittance than RGO in full spectrum, which could make more photons into the surface of $Ag_3PO_4$ to improve photon utilization rate. PL spectra, ns-level time-resolved PL decay spectra, EIS and transient photocurrent responses were employed to investigate the charge transfer process. As shown in Fig. 5c, compared with pristine $Ag_3PO_4$, both $Ag_3PO_4/Ti_3C_2$ and $Ag_3PO_4/RGO$ exhibited substantially depressed PL emissions, indicating pronounced carriers separation [50,51]. To further investigate the photophysical behavior of the photogeneration carriers, the ns-level time-resolved PL

decay spectra of $Ag_3PO_4$, $Ag_3PO_4/RGO$, and $Ag_3PO_4/Ti_3C_2$ were recorded (Fig. 5d). The radiative lifetimes ($\tau$) can be obtained by fitting the decay curves with a biexponential function. As shown in Table S1, The short radiative lifetime ($\tau_1$) of $Ag_3PO_4$ is 1.58 ns, which is decreased down to 1.44 and 1.35 ns in the $Ag_3PO_4/RGO$ and $Ag_3PO_4/Ti_3C_2$ composites, respectively. The long radiative lifetime ($\tau_2$) decreased from 26.61 ns for $Ag_3PO_4$ to 15.44 ns for $Ag_3PO_4/RGO$ and 11.08 ns for $Ag_3PO_4/Ti_3C_2$ composites. This shortened carriers lifetime suggest that an additional nonradiative decay channel may be opened through the electron transfer from $Ag_3PO_4$ to $Ti_3C_2$, which effective suppressed the carrier recombination [52]. EIS Nyquist plots showed that $Ag_3PO_4/Ti_3C_2$ had smallest arc radius (Fig. 5e), which also demonstrated a more effective separation of carriers [53,54]. Furthermore, transient photocurrent responses of $Ag_3PO_4$, $Ag_3PO_4/RGO$ and $Ag_3PO_4/Ti_3C_2$ electrodes were measured to further validate the enhanced carrier separation efficiency in $Ag_3PO_4/Ti_3C_2$ (Fig. 5f). As expected, the photocurrent responses of the $Ag_3PO_4/Ti_3C_2$ electrode was significantly higher than that of $Ag_3PO_4$ and $Ag_3PO_4/RGO$ electrode, indicating an enhanced separation of carriers due to the formation of Schottky junction between $Ti_3C_2$-$Ag_3PO_4$ interface. These results demonstrated that the introduction of $Ti_3C_2$ sheet can remarkably improve the visible light absorption and carrier separation efficiency of $Ag_3PO_4$.

The band structures of as-prepared samples were examined by Mott-Schottky measurement. It is well known that Mott-Schottky analysis is a tool to determine the flat band potential [55,56], which usually is approximate to the conduction band of n-type semiconductors (CB $\approx$ $U_{fb}$ - 0.2 V) [57]. As shown in Fig. S5, the flat-band potential of $Ag_3PO_4$, $Ag_3PO_4/Ti_3C_2$ and $Ag_3PO_4/RGO$ could be extracted from the x-axis intersection and they were approximately 0.2 V, 0.3 V and 0.3 V versus Ag/AgCl, respectively. Thus the conduction band (CB) of $Ag_3PO_4$, $Ag_3PO_4/Ti_3C_2$ and $Ag_3PO_4/RGO$ were O V, 0.1 V and 0.1 V, respectively (equivalent to 0.24 V, 0.34 V and 0.34 V versus NHE, Normal Hydrogen Electrode, respectively). Furthermore, the band gap of $Ag_3PO_4$ evaluated from the Kubelka-Munk method was about 2.42 eV (Fig. S6a). The band structure of $Ag_3PO_4$, $Ag_3PO_4/Ti_3C_2$ and $Ag_3PO_4/RGO$ were presented in Fig. S6b.
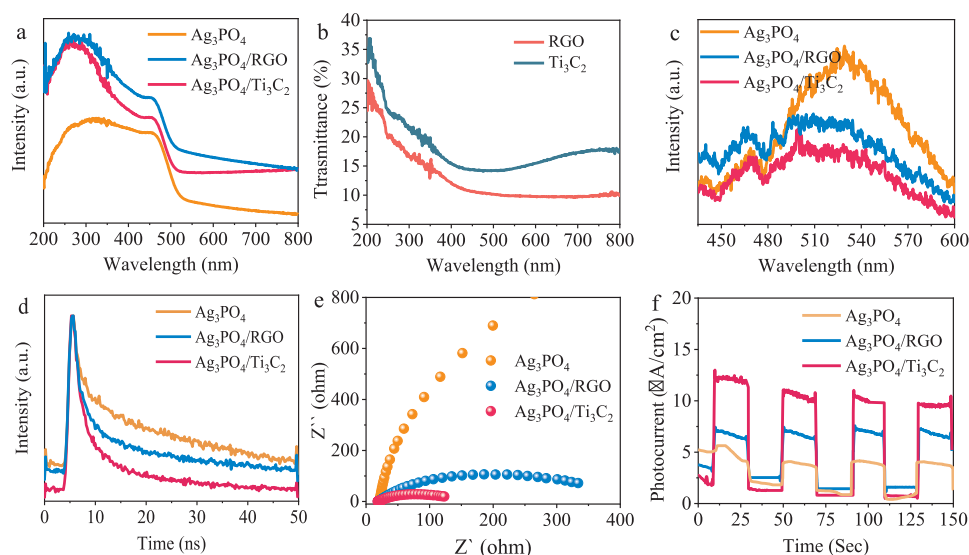
**Fig. 5.** UV–vis diffuse reflectance spectra (a, b), PL spectra (c), time-resolved PL decay spectra (d), EIS Nyquist plots (e) and transient photocurrent responses (f) of as-prepared catalysts.

### 3.3. Photocatalytic degradation of organic pollutants

For simplicity, a model pollutant, methyl orange (MO), was used to optimize the content of $Ti_3C_2$ and RGO in composites. The optimal contents of $Ti_3C_2$ in $Ag_3PO_4/Ti_3C_2$ and RGO in $Ag_3PO_4/RGO$ both were 2 wt.% (Fig. S7). $Ag_3PO_4/Ti_3C_2$ exhibited preferable photocatalytic activities compared with $Ag_3PO_4$ and $Ag_3PO_4/RGO$, which pre-liminarily proved the superiority of $Ag_3PO_4/Ti_3C_2$. Hereafter, only the catalytic activity of optimized $Ag_3PO_4/Ti_3C_2$ and $Ag_3PO_4/RGO$ catalysts were discussed in detail unless otherwise stated.

As mentioned above, a small number of metallic Ag generated in $Ag_3PO_4/Ti_3C_2$ during the synthetic process due to the reduction of $Ag^+$ by low valence Ti species. Thus, to identify the role of metallic Ag in the $Ag_3PO_4/Ti_3C_2$ system, the control experiment was carried out. First, the $Ti_3C_2$ was immersed into $K_2CrO_7$ aqueous solution to consume the low valence Ti species, which get the sample $Ti_3C_2$-R. As shown in Fig. S8, after treatment by $K_2CrO_7$, the peaks corresponding low valence Ti species were completely disappeared, indicating that the low valence Ti species were consumed by $Cr^{6+}$ (electron acceptor). After careful washing with HCl (10 mM) and D.I. water to remove the adsorbed $Cr^{3+}$, and then $Ag_3PO_4/Ti_3C_2$-R can be prepared by above electro-statically driven self-assembly method. As expected, there were no obvious characteristic peaks in connection with metallic Ag appeared in the XRD pattern of $Ag_3PO_4/Ti_3C_2$-R compared with $Ag_3PO_4/Ti_3C_2$ (Fig. S9). Finally, the catalytic activities of $Ag_3PO_4/Ti_3C_2$-R and $Ag_3PO_4/Ti_3C_2$ was compared by the degradation experiment of MO. As shown in Fig. S10, the catalytic activity of $Ag_3PO_4/Ti_3C_2$ is slightly higher than $Ag_3PO_4/Ti_3C_2$-R, which may be caused by the surface plasma resonance of metallic Ag. Since the influence of Ag toward the degradation of MO is relative weak, for simplicity, the role of Ag is ignored in the later discussion.

To investigate the catalytic performance of as-prepared catalysts, typical antibiotic degradation experiments were carried out. Under visible light illumination, all catalysts exhibited vigorous activity to-ward chloramphenicol (CPL) degradation, while the performance of $Ag_3PO_4/Ti_3C_2$ was more prominent (Fig. 6a). To quantify the photo-catalytic activity for different catalysts, the apparent rate constant (k) of CPL ($k_{CPL}$) degradation was calculated with the pseudo-first-order ap-proximation. As shown in Fig. 6b, the $Ag_3PO_4/Ti_3C_2$ gave rise to a $k_{CPL}$ value of 0.025 min$^{-1}$, which is higher than that of $Ag_3PO_4/RGO$ (0.012 min$^{-1}$) and $Ag_3PO_4$ (0.007 min$^{-1}$). Fig. 6c showed the HPLC chromatogram of CPL degradation in $Ag_3PO_4/Ti_3C_2$ system. The CPL

peak (retention time at 4.65 min) became weaker with time and a new peak (retention time at 5.2 min) appeared, indicating that CPL was gradually degraded. The superiority of $Ag_3PO_4/Ti_3C_2$ over the other catalysts in CPL photodegradation was ascribed to the sufficient inter-facial contact, the pronounced charge separation resulting from Schottky junction, and stronger redox reactivity rendered by the surface metal Ti sites on $Ti_3C_2$. Further explanations are shown in the section of mechanism. Thiamphenicol (TPL) (Fig. 6d–f) and tetracycline hydro-chloride (TC-H) (Fig. 6g–i) were also used to further assess the photo-catalytic activity of as-prepared catalysts under visible light. No sur-prisingly, $Ag_3PO_4/Ti_3C_2$ also displayed the highest photocatalytic activity for both TPL and TC-H compared with other catalysts.

A typical persistent organic pollutant 2,4-Dinitrophenol (2,4-DCP) was also employed to evaluate the catalytic activity of as-prepared catalysts. As shown in Fig. S11(a, b), $Ag_3PO_4/Ti_3C_2$ also exhibited ex-cellent performances among them. The $k_{2,4-DNP}$ value degradation with $Ag_3PO_4/Ti_3C_2$ was 2.5 times that of $Ag_3PO_4/RGO$ and 10 times that of $Ag_3PO_4$. The results strongly demonstrated that $Ag_3PO_4/Ti_3C_2$ is an efficient photocatalyst that can degrade most organic pollutants. The apparent rate constant for degradation of various pollutants were shown in Table 1.

### 3.4. Effect of natural organic matters and inorganic salts

Generally, some of the coexisting constituents in the real waste-water, such as inorganic salts [58] and natural organic matter (NOM) [59], can significantly affect the photocatalysis activities of target pollutants. Herein, the proper amounts of humic acid (HA), fulvic acid (FA), $K^+$, $Cr^{6+}$, $SO_4^{2-}$, $H_2PO_4^{2-}$ and $Na^+$ ions (Table S2) were added into TC-H solution respectively to investigate the influence of these constituents for degradation efficiency. As shown in Fig. 7a, both HA and FA had a certain inhibitory effect on TC-H degradation. This can be attributed to the competition between NOM and TC-H, which NOM can scavenge photogenerated holes and radicals [59]. To verify the in-hibitory role of natural organic matter, the generation of ·OH in $Ag_3PO_4/Ti_3C_2$ system under visible light irradiation was detected by ESR. As shown in Fig. S12, when using 5,5-dimethyl-1-pyrroline N-oxide (DMPO) as the spin trap reagent, four characteristic peaks of the DMPO-·OH adducts were detected in $Ag_3PO_4/Ti_3C_2$ system under visible light irradiation, indicating the generation of ·OH. However, in the presence of HA, the production of ·OH was decreased, which reveal that NOM serves as a scavenge of ·OH, thereby retarding the
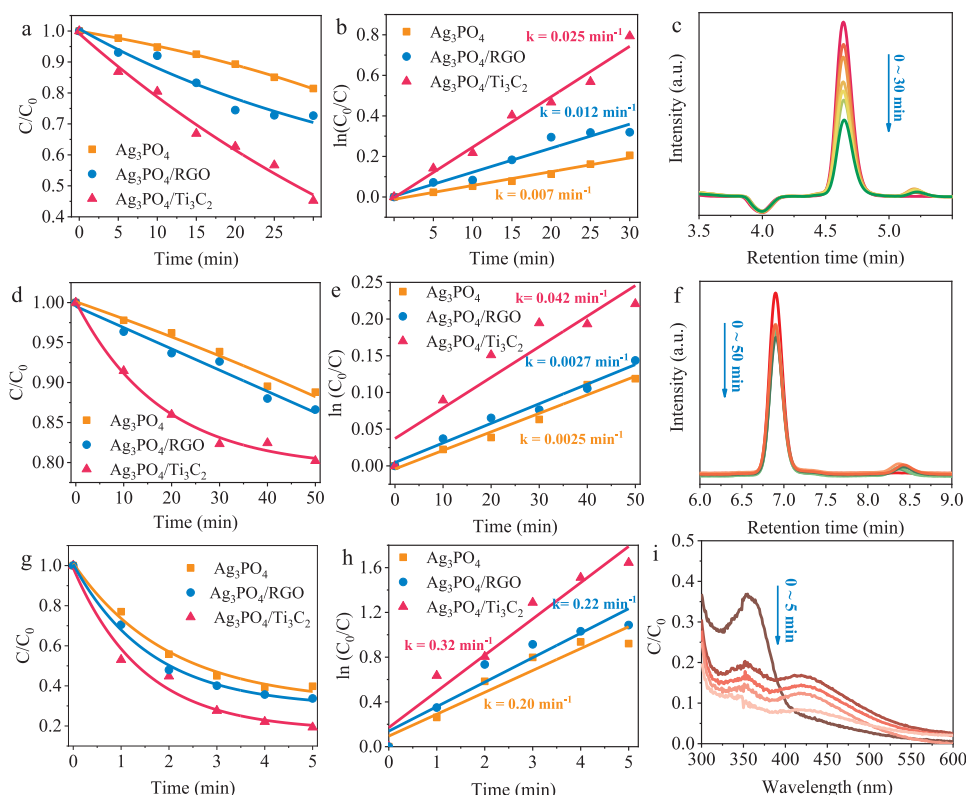
Fig. 6. Photocatalytic degradation of various pollutants by as-prepared catalysts. (a) CPL, (d) TPL and (g) TC-H degradation efficiency in the presence of as-prepared catalysts under visible light irradiation ($\lambda > 420$ nm). The corresponding $\ln(C_0/C)$ vs. reaction time plots of (b) CPL, (e) TPL and (h) TC-H with the fitting results included. HPLC chromatogram of (c) CPL and (f) TPL under different degradation times using as-prepared catalysts. (i) UV–vis absorption spectra of TC-H under different degradation times using different catalysts.

**Table 1**
Degradation details of different pollutants by as-prepared catalysts.

| Pollutants (20 mg/L) | Structure | Catalysts (0.4 g/L) | Rate constants ($min^{-1}$) |
|---|---|---|---|
| MO | | $Ag_3PO_4$ | 0.035 |
| | | $Ag_3PO_4/RGO$ | 0.072 |
| | | $Ag_3PO_4/Ti_3C_2$ | 0.094 |
| 2,4-DNP | | $Ag_3PO_4$ | 0.0005 |
| | | $Ag_3PO_4/RGO$ | 0.002 |
| | | $Ag_3PO_4/Ti_3C_2$ | 0.005 |
| TC-H | | $Ag_3PO_4$ | 0.2 |
| | | $Ag_3PO_4/RGO$ | 0.22 |
| | | $Ag_3PO_4/Ti_3C_2$ | 0.32 |
| TPL | | $Ag_3PO_4$ | 0.0025 |
| | | $Ag_3PO_4/RGO$ | 0.0027 |
| | | $Ag_3PO_4/Ti_3C_2$ | 0.0042 |
| CPL | | $Ag_3PO_4$ | 0.007 |
| | | $Ag_3PO_4/RGO$ | 0.012 |
| | | $Ag_3PO_4/Ti_3C_2$ | 0.025 |

photocatalytic activity toward TC−H. When adding $K_2Cr_2O_7$, $K_2SO_4$ and $NaH_2PO_4$ into reaction solution, respectively, there was no significant difference in the degradation of TC−H, indicating that $K^+$, $SO_4^{2-}$, $Na^+$ $Cr_2O_7^{2-}$ and $H_2PO_4^-$ did not affect the catalytic efficiency of $Ag_3PO_4/Ti_3C_2$ (Fig. 7b). In summary, the catalysis activities of $Ag_3PO_4/Ti_3C_2$ easily influenced by NOM but not $K^+$, $SO_4^{2-}$, $Na^+$ $Cr_2O_7^{2-}$ and $H_2PO_4^{2-}$. Thus, in practical applications, it is necessary to exclude NOM interference through preprocessing.

### 3.5. Stability test

Since the photocorrosion of $Ag_3PO_4$ severely limits its application, the stability test of $Ag_3PO_4$ is necessary, which is one of the important index to evaluate its performance. The anti-photocorrosion

performance of $Ag_3PO_4$, $Ag_3PO_4/RGO$ and $Ag_3PO_4/Ti_3C_2$ was tested through multiple cycles removal of TC-H. An obvious decrease of reaction rate can be observed for both $Ag_3PO_4$ and $Ag_3PO_4/RGO$ (Fig. 8a). Notably, the photocatalytic performance of pure $Ag_3PO_4$ declined by about 92.2% after 8 cycles, indicating a large amount of $Ag_3PO_4$ decomposition caused by photocorrosion. On the contrary, there was a relatively little loss (about 31.6%) in the photocatalytic performance after 8 cycles over $Ag_3PO_4/Ti_3C_2$ composite, suggesting the enhanced anti-photocorrosion performance. XRD patterns of $Ag_3PO_4$, $Ag_3PO_4/RGO$ and $Ag_3PO_4/Ti_3C_2$ after reaction were shown in Fig. 8b. Two peaks at 38.1 and 64.4 eV emerged after reaction, which could be classified as characteristic peaks of silver (JCPDS NO.04-0783). Obviously, the peak intensity was in the order of $Ag_3PO_4 > Ag_3PO_4/RGO > Ag_3PO_4/Ti_3C_2$. It needs to be pointed out that fresh $Ag_3PO_4/Ti_3C_2$ also existed a small amount of metal Ag due to the Ag self-reduction in $Ti_3C_2$ MXene solution. However, no significant change in XRD pattern of $Ag_3PO_4/Ti_3C_2$ before and after reaction indicates that it has good stability. TEM image showed that an amount of metal Ag particles appeared on the surface of $Ag_3PO_4$ (Fig. 8c). HRTEM further showed that the spacing of adjacent lattice planes was ca. 0.236 nm, which can be ascribed to the interplanar spacing of the (111) planes of cubic Ag (inset in Fig. 8c) [57]. However, only a small amount of silver can be found on the surface of $Ag_3PO_4/Ti_3C_2$, indicating its stronger stability. Above results powerfully reveal that $Ag_3PO_4/Ti_3C_2$ sample is more stable than pure $Ag_3PO_4$ and $Ag_3PO_4/RGO$ under the same condition. This is due to the effectively transfer of photoinduced electrons from $Ag_3PO_4$ to $Ti_3C_2$ though Schottky junction, which greatly reduces the possibility of electrons return to $Ag_3PO_4$.

### 3.6. The mechanism of the enhanced photocatalytic performance and stability in $Ag_3PO_4/Ti_3C_2$ Schottky catalyst

Spectroscopic technique combined with band theory were used to investigate the interfacial interactions between $Ti_3C_2$ and $Ag_3PO_4$ before and after Schottky contact. The XPS results (Part 3.1) have
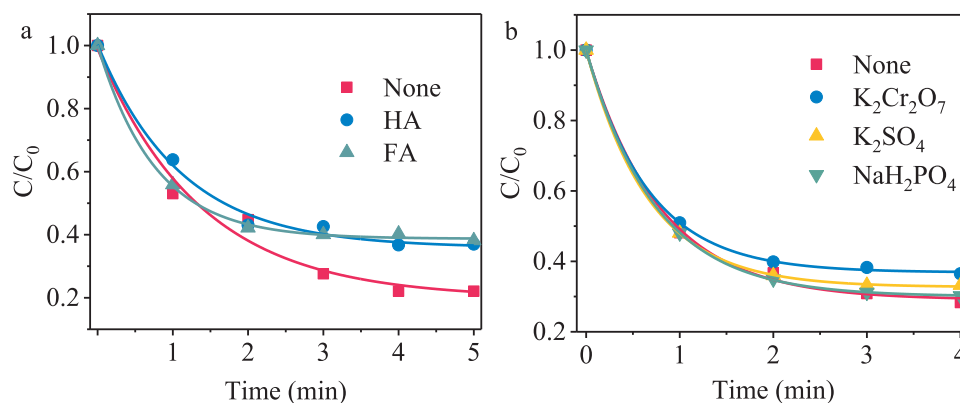
**Fig. 7.** Effects of natural organic matters (a) and inorganic salts (b) to degradation of TC-H.
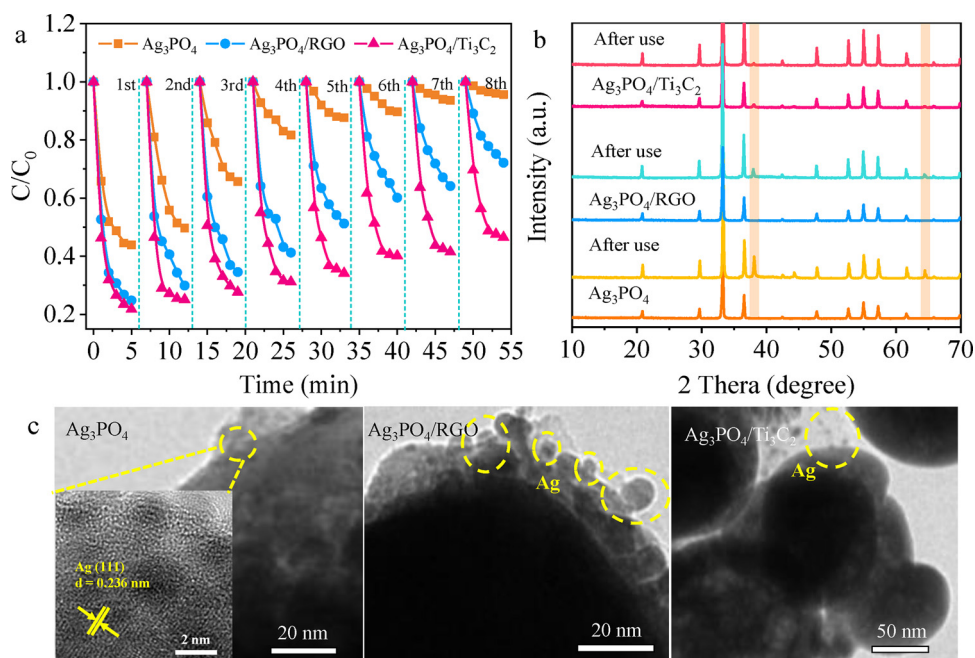


**Fig. 8.** (a) Photodegradation of TC-H for 8 cycles using different catalysts under visible light irradiation (λ > 420 nm). XRD patterns (b) and TEM images (c) of as-prepared catalysts before and after reaction.
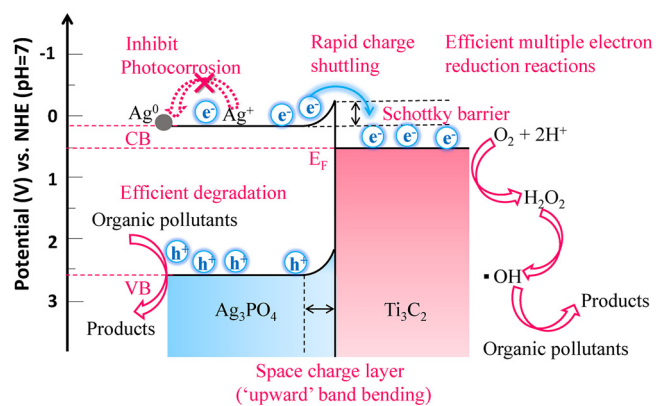


**Fig. 9.** The mechanism of photodegradation and anti-photocorrosion of Ag$_3$PO$_4$/Ti$_3$C$_2$ Schottky catalyst.

demonstrated that electrons are transferred from Ag$_3$PO$_4$ to the Ti$_3$C$_2$ surface after Schottky contact. (Fig. 4C–F). Here, the band theory was employed to further investigate the interfacial interactions between Ti$_3$C$_2$ and Ag$_3$PO$_4$. The Fermi level of Ag$_3$PO$_4$ is higher than that of

Ti$_3$C$_2$, which obtained by above Mott-Schottky measurement (Fig. S5 and Fig. S6b). Thus, the difference of Fermi levels between Ti$_3$C$_2$ and Ag$_3$PO$_4$ drives the electrons flow from Ag$_3$PO$_4$ to Ti$_3$C$_2$ until a uniform Fermi level is formed, followed by band bending and Schottky junction formation (Fig. 9). The XPS results combined with the band theory unequivocal demonstrate that a Schottky junction was formed at the interface of Ti$_3$C$_2$ and Ag$_3$PO$_4$.

The benzoquinone (BQ), Isopropanol (IPA), AgNO$_3$ and Ethylenediaminetetraacetic acid disodium salt (EDTA) were employed as the scavengers for ·O$_2^-$, ·OH, e$^-$ and h$^+$, respectively, to determine the photocatalytic degradation mechanism (Table S3) [60]. As shown in Fig. S13a, the degradation activity was sharply decreased, only when EDTA was added into reaction suspensions, indicating that h$^+$ are main active species for the degradation of TC-H, TPL and CPL. In addition, ·OH also played a weaker role in degradation process. The generation of ·OH was further confirmed by ESR results. As shown in Fig. S13b, the relative intensity of DMPO-·OH signals was in the order of Ag$_3$PO$_4$/Ti$_3$C$_2$ > Ag$_3$PO$_4$/RGO > Ag$_3$PO$_4$. This result may be due to the strong redox reactivity of exposed Ti sites on the surface of Ti$_3$C$_2$, which can promote multiple electron reduction reactions (O$_2$ → H$_2$O$_2$ → ·OH).

According to the above results, we proposed that the mechanism of the enhanced photocatalytic performance and stability in Ag$_3$PO$_4$/Ti$_3$C$_2$

Schottky catalyst (Fig. 9). The enhanced photocatalytic activity and anti-photocorrosion performance of Ag$_3$PO$_4$/Ti$_3$C$_2$ can be attributed to the following reasons: (i) The sufficient and close interfacial contact between Ag$_3$PO$_4$ and Ti$_3$C$_2$ (Figs. 3c and S3c) is beneficial to transfer the carriers (Fig. 5C–F); (ii) the surface metal Ti sites on Ti$_3$C$_2$ with stronger redox reactivity promotes multiple electron reactions (Fig. S13b). (iii) A Schottky junction is formed at Ag$_3$PO$_4$-Ti$_3$C$_2$ interface (Figs. 4C–F and 9), which steers the unidirectional electron flow to be trapped by the Ti$_3$C$_2$ ("electron sink") due to the role of built-in electric field, thereby promoting the separation of carriers.

### 3.7. Ti$_3$C$_2$ as a versatile "electron sink" coupled with other semiconductors

To verify that Ti$_3$C$_2$ could as a versatile "electron sink" coupled with other semiconductors, AgI/Ti$_3$C$_2$ Schottky catalyst was also prepared by a similar method to Ag$_3$PO$_3$/Ti$_3$C$_2$. Morphological structure and crystal structure of AgI/Ti$_3$C$_2$ were provided in Fig S14 and Fig. S15. As shown in Fig. S16 (a, b), the photocatalytic reduction efficiency of AgI/Ti$_3$C$_2$ for Cr$^{6+}$ greatly increased compared with AgI. The apparent rate constant for the reduction of Cr$^{6+}$ using AgI/Ti$_3$C$_2$ was 5 times that of pure AgI. This finding clearly shows an enormous potential in coupling Ti$_3$C$_2$ sheet with a wide variety of semiconductor photocatalysts for more applications.

## 4. Conclusion

Ag$_3$PO$_4$/Ti$_3$C$_2$ Schottky catalyst was synthesized for the first time by electrostatically driven self-assembly strategy successfully. It showed prominent photodegradation performance toward MO, 2,4-DNP, TC-H, TPL and CPL under visible light irradiation. A certain concentration NOM can slightly weaken degradation efficiency because of the competition between NOM and pollutants. Importantly, Ag$_3$PO$_4$/Ti$_3$C$_2$ Schottky catalyst showed excellent stability compared with pure Ag$_3$PO$_4$ and Ag$_3$PO$_4$/RGO. The enhanced photocatalysis activity and anti-photocorrosion performance of Ag$_3$PO$_4$/Ti$_3$C$_2$ can be attributed: the sufficient and close interfacial contact between Ag$_3$PO$_4$ and Ti$_3$C$_2$, unidirectional electron flow to be trapped by the Ti$_3$C$_2$ across the Schottky barrier, and the surface metal Ti sites on Ti$_3$C$_2$ with stronger redox reactivity. Moreover, the efficient photocatalytic reduction of Cr$^{6+}$ in AgI/Ti$_3$C$_2$ system was also achieved, which demonstrated that Ti$_3$C$_2$ can as a versatile "electron sink" for more widely environmental application. This study provide a new idea to improve the photocatalytic activity and anti-photocorrosion performance of photosensitivity semiconductors.

## Acknowledgements

## Appendix A. Supplementary data

Supplementary material related to this article can be found, in the online version, at doi:https://doi.org/10.1016/j.apcatb.2018.08.053.

## References

[1] J. Schneider, M. Matsuoka, M. Takeuchi, J. Zhang, Y. Horiuchi, M. Anpo, D.W. Bahnemann, Chem. Rev. 114 (2014) 9919–9986.
[2] M.R. Hoffmann, S.T. Martin, W. Choi, D.W. Bahnemann, Chem. Rev. 95 (1995) 69–96.
[3] C. Li, Y. Xu, W. Tu, G. Chen, R. Xu, Green Chem. 19 (2017) 882–899.
[4] N. Shao, J. Wang, D. Wang, P. Corvini, Appl. Catal B Environ. 203 (2017) 964–978.
[5] H. Dong, G. Chen, J. Sun, C. Li, Y. Yu, D. Chen, Appl. Catal. B Environ. 134 (2013) 46–54.
[6] H. Dong, G. Chen, J. Sun, Y. Feng, C. Li, C. Lv, Chem. Commun. 50 (2014) 6596–6599.
[7] H. Dong, G. Chen, J. Sun, C. Li, Y. Hu, Z. Han, Inorg. Chem. 54 (2015) 11826–11830.
[8] H. Dong, G. Chen, J. Sun, Y. Feng, C. Li, G. Xiong, C. Lv, J. Chem. Soc. Dalton Trans. 43 (2014) 7282–7289.
[9] H. Dong, J. Sun, G. Chen, C. Li, Y. Hu, C. Lv, PCCP 16 (2014) 23915–23921.
[10] C. Li, S. Yu, Y. Wang, J. Han, H. Dong, G. Chen, J. Taiwan Inst. Chem. E. 87 (2018) 272–280.
[11] J. Guo, S. Ouyang, P. Li, Y. Zhang, T. Kako, J. Ye, Appl. Catal. B Environ. 134-135 (2013) 286–292.
[12] Z.-M. Yang, G.-F. Huang, W.-Q. Huang, J.-M. Wei, X.-G. Yan, Y.-Y. Liu, C. Jiao, Z. Wan, A. Pan, J. Mater. Chem. A 2 (2014) 1750–1756.
[13] Z. Yi, J. Ye, N. Kikugawa, T. Kako, S. Ouyang, H. Stuart-Williams, H. Yang, J. Cao, W. Luo, Z. Li, Y. Liu, R.L. Withers, Nat. Mater. 9 (2010) 559–564.
[14] J. Guo, H. Zhou, S. Ouyang, T. Kako, J. Ye, Nanoscale 6 (2014) 7303–7311.
[15] Q. Xiang, D. Lang, T. Shen, F. Liu, Appl. Catal. B Environ. 162 (2015) 196–203.
[16] X. Yang, H. Cui, Y. Li, J. Qin, R. Zhang, H. Tang, ACS Catal. 3 (2013) 363–369.
[17] L. Liu, J. Liu, D.D. Sun, Catal. Sci. Technol. 2 (2012) 2525.
[18] X. Lin, X. Guo, W. Shi, F. Guo, G. Che, H. Zhai, Y. Yan, Q. Wang, Catal. Commun. 71 (2015) 21–27.
[19] Y. He, L. Zhang, B. Teng, M. Fan, Environ. Sci. Technol. 49 (2015) 649–656.
[20] X. Miao, X. Yue, Z. Ji, X. Shen, H. Zhou, M. Liu, K. Xu, J. Zhu, G. Zhu, L. Kong, Appl. Catal. B: Environ. 227 (2018) 459–469.
[21] Y. Bi, S. Ouyang, J. Cao, J. Ye, Phys. Chem. Chem. Phys. 13 (2011) 10071–10075.
[22] S. Huang, Y. Xu, T. Zhou, M. Xie, Y. Ma, Q. Liu, L. Jing, H. Xu, H. Li, Appl. Catal. B Environ. 225 (2018) 40–50.
[23] A.K. Geim, Science 324 (2009) 1530–1534.
[24] J. Yuan, X. Liu, Y. Tang, Y. Zeng, L. Wang, S. Zhang, T. Cai, Y. Liu, S. Luo, Y. Pei, Appl. Catal. B Environ. 237 (2018) 24–31.
[25] Q. Lin, L. Li, S. Liang, M. Liu, J. Bi, L. Wu, Appl. Catal. B Environ. 163 (2015) 135–142.
[26] L. Liu, Y. Qi, J. Lu, S. Lin, W. An, Y. Liang, W. Cui, Appl. Catal. B Environ. 183 (2016) 133–141.
[27] Y. Hernandez, V. Nicolosi, M. Lotya, F.M. Blighe, Z. Sun, S. De, I.T. McGovern, B. Holland, M. Byrne, Y.K. Gun'Ko, J.J. Boland, P. Niraj, G. Duesberg, S. Krishnamurthy, R. Goodhue, J. Hutchison, V. Scardaci, A.C. Ferrari, J.N. Coleman, Nat. Nanotechnol. 3 (2008) 563–568.
[28] P. Simon, ACS Nano 11 (2017) 2393–2396.
[29] Y. Dong, Z.S. Wu, S. Zheng, X. Wang, J. Qin, S. Wang, X. Shi, X. Bao, ACS Nano 11 (2017) 4792–4800.
[30] M. Naguib, J. Halim, J. Lu, K.M. Cook, L. Hultman, Y. Gogotsi, M.W. Barsoum, J. Am. Chem. Soc. 135 (2013) 15966–15969.
[31] M.R. Lukatskaya, O. Mashtalir, C.E. Ren, Y. Dall'Agnese, P. Rozier, P.L. Taberna, M. Naguib, P. Simon, M.W. Barsoum, Y. Gogotsi, Science 341 (2013) 1502–1505.
[32] B. Anasori, M.R. Lukatskaya, Y. Gogotsi, Nat. Rev. Mater. 2 (2017) 16098.
[33] J. Ran, G. Gao, F.T. Li, T.Y. Ma, A. Du, S.Z. Qiao, Nat. Commun. 8 (2017) 13907.
[34] G. Gao, A.P. O'Mullane, A. Du, ACS Catal. 7 (2016) 494–500.
[35] M. Ghidiu, M.R. Lukatskaya, M.-Q. Zhao, Y. Gogotsi, M.W. Barsoum, Nature 516 (2014) 78.
[36] Z. Zhuang, Y. Li, Z. Li, F. Lv, Z. Lang, K. Zhao, L. Zhou, L. Moskaleva, S. Guo, L. Mai, Angew. Chem. Int. Ed. 130 (2017) 505–509.
[37] F. Liu, A. Zhou, J. Chen, J. Jia, W. Zhou, L. Wang, Q. Hu, Appl. Surf. Sci. 416 (2017) 781–789.
[38] O. Mashtalir, M. Naguib, V.N. Mochalin, Y. Dall'Agnese, M. Heon, M.W. Barsoum, Y. Gogotsi, Nat. Commun. 4 (2013) 1716.
[39] D.C. Marcano, D.V. Kosynkin, J.M. Berlin, A. Sinitskii, Z. Sun, A. Slesarev, L.B. Alemany, W. Lu, J.M. Tour, ACS Nano 4 (2010) 4806–4814.
[40] Y. Choi, M.S. Koo, A.D. Bokare, D.H. Kim, D.W. Bahnemann, W. Choi, Environ. Sci. Technol. 51 (2017) 3973–3981.
[41] M. Naguib, M. Kurtoglu, V. Presser, J. Lu, J. Niu, M. Heon, L. Hultman, Y. Gogotsi, M.W. Barsoum, Adv. Mater. 23 (2011) 4248–4253.
[42] Q. Liang, Y. Shi, W. Ma, Z. Li, X. Yang, PCCP 14 (2012) 15657–15665.
[43] G. Zou, Z. Zhang, J. Guo, B. Liu, Q. Zhang, C. Fernandez, Q. Peng, ACS Appl. Mater. Interfaces 8 (2016) 22280–22286.
[44] Z. Zhang, H. Li, G. Zou, C. Fernandez, B. Liu, Q. Zhang, J. Hu, Q. Peng, ACS Sustain. Chem. Eng. 4 (2016) 6763–6771.
[45] N. Kurra, B. Ahmed, Y. Gogotsi, H.N. Alshareef, Adv. Energy Mater. 6 (2016) 1601372.
[46] Q. Xue, H. Zhang, M. Zhu, Z. Pei, H. Li, Z. Wang, Y. Huang, Y. Huang, Q. Deng, J. Zhou, S. Du, Q. Huang, C. Zhi, Adv. Mater. 29 (2017) 1604847.
[47] S. Cao, B. Shen, T. Tong, J. Fu, J. Yu, Adv. Funct. Mater. 28 (2018) 1800136.
[48] T.Y. Ma, J.L. Cao, M. Jaroniec, S.Z. Qiao, Angew. Chem. Int. Ed. 55 (2016) 1138–1142.
[49] J. Low, L. Zhang, T. Tong, B. Shen, J. Yu, J. Catal. 361 (2018) 255–266.
[50] C. Li, G. Chen, J. Sun, H. Dong, Y. Wang, C. Lv, Appl. Catal. B Environ. 160 (2014) 383–389.
[51] C. Li, G. Chen, J. Sun, J. Rao, Z. Han, Y. Hu, W. Xing, C. Zhang, Appl. Catal. B Environ. 188 (2016) 39–47.
[52] C. Li, Y. Du, D. Wang, S. Yin, W. Tu, Z. Chen, M. Kraft, G. Chen, R. Xu, Adv. Funct. Mater. 27 (2017) 1604328.
[53] T. Yan, J. Tian, W. Guan, Z. Qiao, W. Li, J. You, B. Huang, Appl. Catal. B Environ. 202 (2017) 84–94.
[54] C. Li, G. Chen, J. Sun, Y. Feng, J. Liu, H. Dong, Appl. Catal. B Environ. 163 (2015) 415–423.
[55] J. Liu, C. Zhang, B. Ma, T. Yang, X. Gu, X. Wang, J. Zhang, C. Hu, Nano Energy 38

(2017) 271–280.

[56] Q. Li, Y. Xia, C. Yang, K. Lv, M. Lei, M. Li, Chem. Eng. J. 349 (2018) 287–296.

[57] T. Cai, Y. Liu, L. Wang, S. Zhang, Y. Zeng, J. Yuan, J. Ma, W. Dong, C. Liu, S. Luo, Appl. Catal. B Environ. 208 (2017) 1–13.

[58] X. Hua, F. Teng, Y. Zhao, J. Xu, C. Xu, Y. Yang, Q. Zhang, S. Paul, Y. Zhang,

M. Chen, X. Zhao, Water Res. 81 (2015) 366–374.

[59] M. Long, J. Brame, F. Qin, J. Bao, Q. Li, P.J. Alvarez, Environ. Sci. Technol. 51 (2016) 514–521.

[60] P. Zhou, J. Yu, M. Jaroniec, Adv. Mater. 26 (2014) 4920–4935.